Analysis of the reconstructed Ir(110) surface from time-of-flight scattering and recoiling spectrometry

M. Shi, H. Bu, and J. W. Rabalais
Department of Chemistry, University of Houston, Houston, Texas 77204-5641
(Received 12 February 1990; revised manuscript received 29 March 1990)

Time-of-flight scattering and recoiling spectrometry and low-energy electron diffraction are used to analyze the reconstructed Ir(110) surface. The structure is determined from scans of (i) backscattering (BS) versus incident angle α, (ii) forward scattering (FS) versus α, and (iii) FS versus scattering angle θ along different azimuths δ with use of a pulsed 4-keV Ar^+-primary-ion beam. Plots of BS intensities in (α,δ) space provide scattering structural contour maps that expose the surface symmetry. Measurements of BS intensities as a function of α along the $[1\bar{1}0]$ azimuth, where the interatomic spacings are not affected by reconstruction, are used to obtain experimental points on the shadow cones. These points are used to calibrate the screening constant of the interatomic potential used in the trajectory simulations. The experimental data and calibrated simulations are applied to an analysis of the surface reconstruction. The results are consistent with a model in which the reconstructed surface consists of primary domains of faceted (1×3) structures (with two missing first-layer rows and one missing second-layer row) along with secondary domains of (1×1) structures (with no missing rows). Estimates of the interatomic spacings in the (1×3) domains indicate that the second-layer atoms are shifted from the bulk values laterally by $\sim6\%$ towards the center of the trough and that the first- to second-layer spacing is contracted by $\sim8\%$.

I. INTRODUCTION

Reconstruction of the (110) surfaces of fcc transition metals into missing-row structures is a well-known phenomenon.[1] The clean (110) surfaces of 5*d* metals such as Au, Pt, and Ir are reconstructed at room temperature, whereas reconstruction can be induced in the surfaces of 3*d* and 4*d* metals by adsorption of alkali metals.[2,3] Recent total-energy calculations[4–7] on Au(110) suggest that the reconstruction is driven by the need to reduce the high energy of the surface *s-p* electrons. This high energy results from confinement of the *s-p* electrons into a small effective volume which is determined by the lattice dimensions and the large 5*d* orbitals. This confinement is not as restrictive in the first- and second-row transition metals due to the smaller size of the 3*d* and 4*d* orbitals. Reconstruction reduces the confinement and, thus, the energy of the *s-p* electrons. The calculations show lower energies for the reconstructed (1×2) surface than for the unreconstructed (1×1) surface. The energies of some of the higher-order reconstructions, e.g., $(1\times n)$, where $n>2$, are calculated to be lower than that of the (1×2) surface. In these higher-order structures, additional rows of atoms are missing from the surface and subsurface layers, forming large microfacets normal to the [111] direction.

Such reconstructions of Au, Pt, and Ir have been studied by a variety of techniques, including low-energy electron diffraction (LEED),[8–10] field-ion microscopy (FIM),[11] ion scattering,[12–16] x-ray analysis,[17] electron microscopy,[18] and scanning tunneling microscopy.[19] The (1×2) "missing-row" reconstruction has been documented and (1×3) reconstruction has been observed for surfaces with adsorbates for both Pt and Au.[2,8–10] It has generally been accepted that Ir undergoes a (1×2) reconstruction; the evidence for this was not completely clear. LEED work reports[9,10] imperfect (1×2) structures which are streaked, elongated, or with "extra" spots along the [001] direction. FIM work[11] shows that before a (1×2) structure is formed, the plane may be intermixed with atomic rows separated by single or double [001] spacings. In recent work on Ir(110) by Hetterich and Heiland,[20] it was shown that the LEED patterns were neither (1×2) nor (1×3) but could possibly be reconciled by a mixture of the two and that the ion-scattering results indicated that the most important structural elements were $[1\bar{1}0]$ rows and (1×3) troughs. Using time-of-flight scattering and recoiling spectrometry (TOF-SARS), we have recently[21] confirmed these findings of two missing rows and extended the model to include adjacent first-layer rows, hence a mixed faceted (1×3) and (1×1) structure. This model consists of primary domains of (1×3) structures with two missing first-layer rows and one missing second-layer row coexisting with secondary domains of (1×1) structures with two or more adjacent first-layer rows. A schematic drawing of the Ir(110) surface, showing the faceted (1×3) structure and (1×1) structures, is shown in Fig. 1 along with the angular notation.

An ongoing project[22–25] in this laboratory is the TOF-SARS determination of the chemisorption structures of O_2 and H_2 gases on such "row-trough" surfaces. Analysis of the clean surface structure is necessary for the determination of these adsorbate structures. The purpose of this paper is to present an analysis of the mixed faceted (1×3) and (1×1) Ir(110) structure as determined from TOF-SARS. This structure is determined from

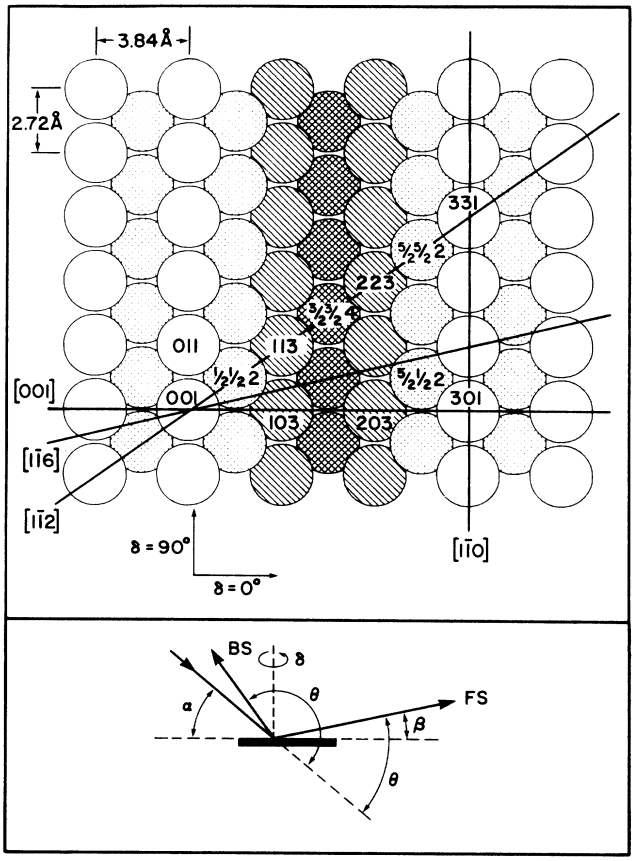

FIG. 1. Reconstructed Ir(110) surface showing coexisting faceted (1×3) and (1×1) structures. Open circles, first layer; dotted circles, second layer; dashed circles, third layer; hatched circles, fourth layer. The nomenclature for the atomic positions is indicated. The angular notation used in TOF-SARS is shown in the lower figure.

both backscattering (BS) and forward-scattering (FS) spectra as a function of beam incident α, exit β, and scattering θ angles and crystal azimuthal δ angle. Classical trajectories along with shadowing and blocking cones are calculated from calibrated interatomic potentials and used to interpret the scattering structures.

The paper is organized as follows. The TOF-SARS technique is briefly described along with the sample cleaning procedure in Sec. II. Details of the experimental results and interpretations of the LEED and TOF-SARS measurements are presented in Sec. III. Section IV contains a qualitative description of the reconstruction models considered and their agreement with the experimental results, while Sec. V provides an estimate of the interatomic spacings. Sections VI and VII provide a discussion and summary of the findings.

II. EXPERIMENTAL METHODS

The TOF-SARS technique and applications to structural analysis have been described elsewhere.[22,26] The experimental parameters used herein were as follows: pulsed 4-keV Ar^+-primary-ion beam; pulse width ~30 nsec; pulse rate ~30 kHz; average current density 0.05–0.1 nA/mm^2. A TOF spectrum of scattered neutrals plus ions can be acquired with a dose of $\approx 10^{-4}$ ion per target-atom. The measurements were made in the new TOF-SARS chamber[26] with base pressure of 1×10^{-10} Torr and a variable scattering angle for both backscattering (BS) and forward scattering (FS). LEED measurements were made with *in situ* reverse-view hemispherical grid optics.

The Ir sample was in the form of a disk 1 mm thick and 10 mm in diameter which was oriented to $<0.5°$. It was mechanically polished with successively finer grits of alumina down to 0.05 μm and mounted on a precision manipulator that allowed both polar incident and azimuthal rotations, translations along three orthogonal axes, and adjustment of the sample tilt angle with respect to the incident ion beam. The beam incident angle α and the scattering angle θ were aligned by means of a laser beam. The LEED pattern was used for coarse alignment of the azimuthal angle δ and surface semichanneling[26] of the Ar^+ beam was used for precise alignment along the [001] and [1$\bar{1}$0] directions. The resulting accuracy was $\pm1°$ for α, θ, and δ, although the reproducibility of these angular positions was $<\pm0.5°$. The crystal was cleaned by Ar^+ sputtering and O_2 treatment cycles followed by annealing to 1400 °C by electron bombardment from the back side. Temperature was measured by means of a portable infrared thermometer. Cleanliness was verified by the absence of carbon and oxygen Auger signals and the absence of H, C, and O recoils[27] in the FS spectra. All measurements were made after annealing to 1400 °C and cooling to room temperature.

TOF spectra were collected by counting for periods of typically 20 sec. Both backscattering and forward-scattering intensities [I(BS) and I(FS)] versus α scans were obtained by fixing θ and δ and rotating the crystal along an axis contained by the surface plane and perpendicular to the scattering plane so as to vary α. Scans of I(FS) versus β were obtained by fixing α and δ and varying θ by moving the detector; the exit angle is then $\beta=\theta-\alpha$. Scans of I(BS) versus δ were obtained by fixing α and θ and rotating the crystal about the surface normal. The angle α was varied from 0° (ion beam parallel to crystal surface) up to 90° in 1° or 2° increments. Such α scans were made along different azimuths in increments of 6°, where $\delta=0°$ corresponds to the [001] azimuth and $\delta=90°$ corresponds to the [1$\bar{1}$0] azimuth. The crystal was annealed following each scan in order to avoid contamination and surface damage. Since the α scans were made on different days, it was difficult to establish exactly the same conditions, therefore it was necessary to calibrate the intensities along different azimuths. This was accomplished by performing δ scans at different α values and using these to normalize the previous α scans.

III. EXPERIMENTAL RESULTS AND INTERPRETATIONS

A. Low-energy electron diffraction pattern

The LEED pattern observed for Ir(110) after cleaning and annealing to 1400 °C is shown in Fig. 2. The pattern

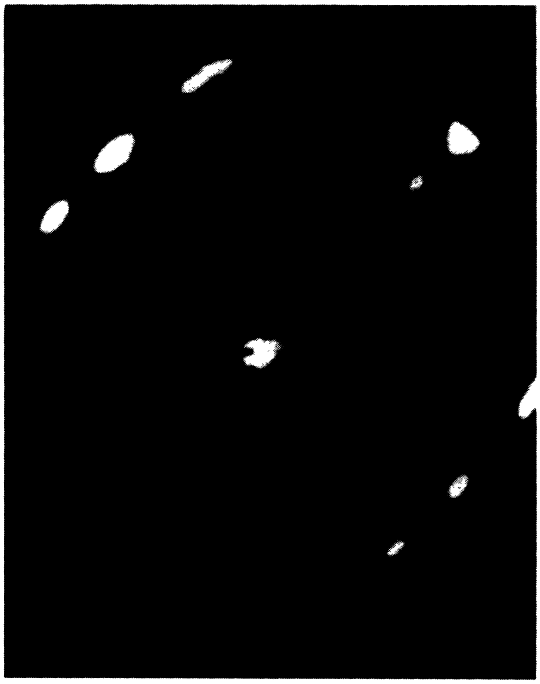

FIG. 2. LEED pattern observed for clean Ir(110) after annealing to 1400 °C.

exhibits "streaky" and elongated spots in the [001] direction as observed by others.[10,20] Neither a pure (1×2) nor (1×3) structure is supported by this pattern. As suggested previously,[20] the pattern may represent a mixture of coexisting domains, however, we are not equipped for quantitative LEED analysis.

B. Time-of-flight spectra

Examples of TOF spectra of scattered neutrals plus ions for FS and BS scattering angles θ are shown in Fig. 3. The sharp peaks correspond to Ar quasi-single-scattering (SS) from Ir while the broad structures correspond to quasi-multiple-scattering (MS) from two or more Ir atoms. The TOF peaks are identified by application of the classical binary elastic collision model.[27] The absence of H, C, and O recoils in FS spectra confirms the surface cleanliness.

The position of the sharp peaks for $\theta > 60°$ are independent of the α and δ orientations of the sample and very close to the TOF predicted by the binary elastic collision model, indicating that the major contribution to these peaks is SS. MS sequences with high energies are observed on the low TOF side of the SS peak for $\theta < 150°$. Broad, low-energy tails are observed on all of the spectra, extending to high TOF; these tails correspond to MS sequences in which the projectile has suffered large energy losses. For $\theta < 60°$, the SS and MS peaks overlap and cannot be resolved in TOF; these peaks are not used for quantitative analysis. I(BS) and I(FS) were taken as the integrated counts in a 0.3 μsec window centered at the SS peak maximum following background subtraction. For the TOF spectra used for quantitative analysis, the MS contributions at the SS position were always $< 10\%$ for I(BS) and $< 30\%$ for I(FS).

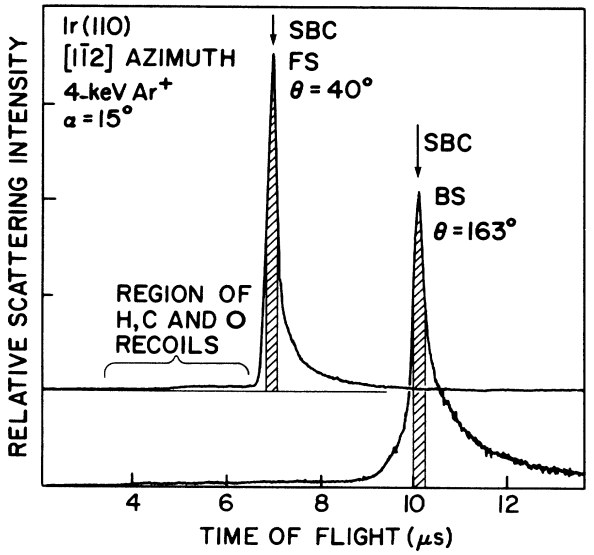

FIG. 3. Examples of backscattering (BS) and forward-scattering (FS) TOF spectra for 4-keV Ar^+ scattering from a clean Ir(110) surface for two different scattering angles. The areas measured as Ar BS intensity, I(BS), and FS intensity, I(FS), are shown hatched. The spectral region for impurity H, C, and O recoils is indicated. The positions corresponding to quasi-single-binary collisions (SBC) with Ir are indicated.

C. Backscattering intensity I(BS) versus incident angle α scans

I(BS) as a function of α was measured along different azimuths δ for $\theta = 163°$. In this *shadowing mode*, I(BS) is determined by the ability of the incident ions to make almost head-on collisions with Ir atoms. Because of shadowing effects, the trajectories are focused at the edge of the shadow cones. At a critical incident angle α_c, where the edge of the cone coincides with a neighboring atom, large enhancements in I(BS) are observed.[22] Selected I(BS) versus α scans are shown in Fig. 4. For each major peak, the α_c's for all possible shadowing and scattering atom combinations[22] are calculated, assuming (1×3), (1×2), and (1×1) structures. Details of the calculation will be presented in Sec. V. Table I summarizes the results.

1. α scan along [1$\bar{1}$0] azimuth, $\delta = 90°$

I(BS) is very low for $\alpha < 15°$, indicating that the surface is well ordered along this azimuth. From Fig. 1 it is observed that the first through fourth layers present identical atomic spacings to the incoming beam, resulting in contributions from all of these layers at the same α. The intense peak at $\alpha = 28°$ results from atoms emerging from shadow cones of their nearest neighbors in the same layer, such as (011) atoms emerging from cones of (001) atoms. The peak at $\alpha = 60°$ results from interactions of neighboring atoms in different layers such as (001)-(013). The intensity of this peak is low because it results from MS sequences. The SS trajectories are blocked by atoms

residing directly above the target atoms, e.g., scattering from (013) is blocked by (011). Scattering along this azimuth provides no information concerning a possible $(1\times n)$ reconstruction.

2. α scan along [001] azimuth, $\delta=0°$

The significant I(BS) observed at very low α, i.e., $<5°$, indicates that there is disorder along this azimuth. The first α_c position at 6° corresponds to first-layer interactions such as (001)-(301) occurring at interatomic distances >11 Å. Although α_c has poor sensitivity to changes in such large interatomic spacings, the result is in qualitative agreement with the structure of Fig. 1. The structure at $\alpha<15°$ is broad because interactions such as $(\frac{1}{2}\,\frac{1}{2}\,2)$-$(\frac{5}{2}\,\frac{1}{2}\,2)$ produce slightly higher α_c's which are not resolved from the (001)-(301) peak. The intense peak at $\alpha=23°$ results from three types of contributions: (i) (001)-(303), (ii) $(\frac{5}{2}\,\frac{1}{2}\,2)$-$(\frac{7}{2}\,\frac{1}{2}\,2)$, and (iii) (301)-(401). Contribution (i) results only from (1×3) structures, contribution (iii) results only from (1×1) structures, and contribution (ii) results from both (1×3) and (1×1) structures. The 29° peak corresponds to shadowing across the trough onto third- and fourth-layer atoms, e.g., (001)-(203) and $(\frac{1}{2}\,\frac{1}{2}\,2)$-$(\frac{5}{2}\,\frac{1}{2}\,4)$ interactions. The 49° peak corresponds to shadowing from the near side of the trough onto third- and fourth-layer atoms, e.g., (001)-(103) and $(\frac{1}{2}\,\frac{1}{2}\,2)$-$(\frac{3}{2}\,\frac{1}{2}\,4)$. The peak at 39° is attributed to scattering from deeper layers for the following reasons. (i) As θ is decreased, the peak decreases in intensity and disappears completely at $\theta=115°$, while there are no changes in other features. The reason for this is that scattering trajectories from the fifth- through seventh-layers can escape for high-angle BS such as $\theta=163°$ but are blocked by first- through fourth-layer atoms for $\theta=115°$, where the outgoing trajectories are near the surface normal. (ii) The structure is absent for the (1×2) missing row reconstruction of Pt(110).[21] The reason for this is that the (1×3) faceted structure is considerably more open than the (1×2) structure of Pt(110), thus facilitating deep layer scattering in the former.

3. α scan along [1$\bar{1}$2] azimuth, $\delta=35.3°$

Along this azimuth atoms from all layers are aligned in the scattering plane. The assignments of the structures

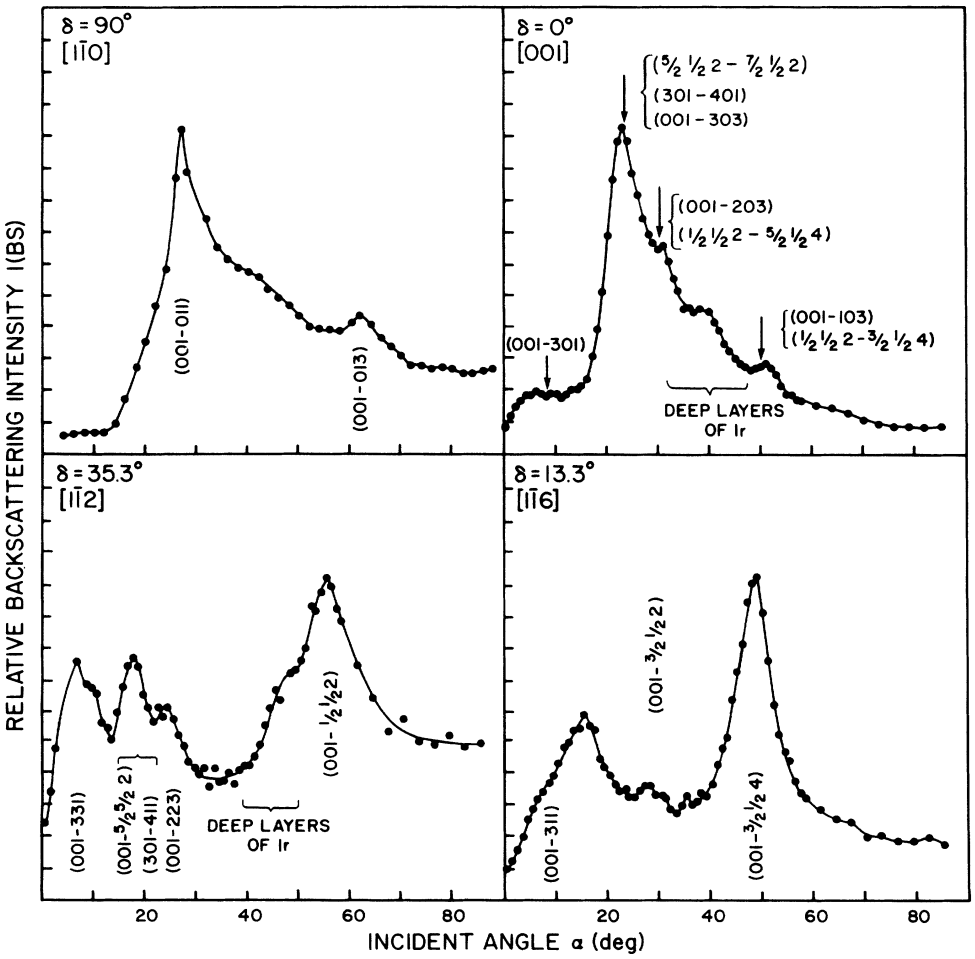

FIG. 4. I(BS) vs incident angle α scans for Ir(110) along four different azimuths δ. The calculated α_c positions for a faceted (1×3) structure are shown. These positions are labeled with the identities of the two atoms involved in the shadowing and scattering.

are listed in Table I. The 17° peak can result from both (1×3) and (1×1) structures. For the 60° peak, contributions from all three listed interactions occur at the same angle if the interlayer spacings are all equal. If these spacings differ because of relaxation effects, the α_c's will be only slightly different and not resolvable. The shoulder near 50° is identified as deep layer scattering since it disappears as θ is reduced from 163° to 115°.

4. *α scan along [1$\bar{1}$6] azimuth, δ=13.3°*

Two major peaks are observed with α_c's $\approx$6° and 45°, which result from the two atoms aligned in the scattering plane along this azimuth, i.e., (311) and ($\frac{3}{2}\frac{1}{2}$4). A very low-intensity peak is observed at $\approx$27°; this is a major peak[21] in the (1×2) missing row Pt(110) structure, i.e., its intensity is comparable to the 45° peak. It arises from

TABLE I. Experimental α_c's and corresponding shadowing and scattering atom pairs along with calculated α_c's for a mixed [(1×3)+(1×1)] structure and a (1×2) structure.

Azimuth	α_c (expt)	Shadowing atom	Scattering atom	Calculated[a] [(1×3)+(1×1)]	α_c's (1×2)
[1$\bar{1}$0]	22.7°	(001)	(011)		
		($\frac{1}{2}\frac{1}{2}$2)	($\frac{1}{2}\frac{3}{2}$2)	22.9°	22.9°
		(103)	(113)		
		($\frac{3}{2}\frac{1}{2}$4)	($\frac{3}{2}\frac{3}{2}$4)		
	60.0°	(001)	(013)		
		($\frac{1}{2}\frac{1}{2}$2)	($\frac{1}{2}\frac{3}{2}$4)	62.4°	62.4°
		(103)	(115)		
		($\frac{3}{2}\frac{1}{2}$4)	($\frac{3}{2}\frac{3}{2}$6)		
[001]	6.0°[c]	(001)	(301)	7.2°	
		(001)	(201)		10.0°[b]
	19.6°	($\frac{5}{2}\frac{1}{2}$2)	($\frac{7}{2}\frac{1}{2}$2)		
		(301)	(401)	17.4°	17.4°
		(001)	(303)	20.3°	
	30.0°	(001)	(203)	29.1°	29.1°
		($\frac{1}{2}\frac{1}{2}$2)	($\frac{5}{2}\frac{1}{2}$4)		
	38.0°		5th–7th layers	33.0°	
	49.5°	(001)	(103)	50.1°	50.1°
		($\frac{1}{2}\frac{1}{2}$2)	($\frac{3}{2}\frac{1}{2}$4)		
[1$\bar{1}$2]	5.0°[c]	(001)	(331)	6.1°	
		(001)	(221)		8.4°[b]
	15.0°[c]	(001)	($\frac{5}{2}\frac{5}{2}$2)	13.8°	
		(301)	(411)	14.8°	
		(001)	($\frac{3}{2}\frac{3}{2}$2)		21.4°[b]
	23.0°	(001)	(223)	24.2°	
	50.0°	(001)	($\frac{1}{2}\frac{1}{2}$2)		
		($\frac{1}{2}\frac{1}{2}$2)	(113)	53.0°	53.0°
		(113)	($\frac{3}{2}\frac{3}{2}$4)		
[1$\bar{1}$6]	8.0°	(001)	(311)	7.1°	7.1°
		(001)	($\frac{3}{2}\frac{1}{2}$2)		25.0°[b]
	44.2°	(001)	($\frac{3}{2}\frac{1}{2}$4)	45.1°	45.1°

[a]The calculated α_c's were determined from the bulk interatomic spacings.
[b]These scattering peaks are not observed in Ir(110) but are observed (Refs. 13 and 21) in Pt(110), which is a (1×2) reconstructed surface.
[c]These α_c's are difficult to measure and contain higher than normal uncertainties due to problems such as extremely low α_c's, deep layer contributions, and/or overlapping peaks.

first-layer (001) atoms shadowing second-layer ($\frac{3}{2}\,\frac{1}{2}\,2$) atoms across a trough which has only one missing first-layer row. These ($\frac{3}{2}\,\frac{1}{2}\,2$) atoms are completely missing in the (1×3) structure. This low-intensity peak observed in Fig. 4 can result from both traces of (1×2) structures and/or (1×1) structural domains such as (301)-($\frac{9}{2}\,\frac{1}{2}\,2$).

D. Scattering structural contour map (SSCM)

The I(BS) versus α scans are collected as SSCM's in Fig. 5. The scans were acquired at increments of $\alpha=2°$ and $\delta=6°$ and an interpolation routine was used to generate the smooth curves of Fig. 5. The SSCM's provide the following information. (i) They are a concise summary of all the I(BS) versus α scans. (ii) They reveal the symmetry of the I(BS) data in (α,δ) space. (iii) They provide a characteristic fingerprint for a surface, revealing its general features which serve as a guide for more detailed studies of reconstruction. (iv) Comparison of the clean surface SSCM to that of the adsorbate covered SSCM reveals adsorbate-induced structural changes and provides insight into the position of the adsorption site.

Figure 5 reveals the following points. (i) The SSCM contours illustrate the general symmetry about the $\delta=0°$ and 90° directions, confirming the high lattice symmetry about the [001] and [1$\bar{1}$0] azimuths. Close observation shows that I(BS) is not perfectly symmetrical about these azimuths, particularly at high α, where I(BS) is low. This is due to the uncertainties in calibrating some thirty different α scans taken over a period of several days; the calibration introduces $\approx 15\%$ error and the ion-beam current is stable to within $\approx 10\%$. Thus, whereas the positions of the peaks are symmetrical, the absolute intensities exhibit some variations. (ii) I(BS) starts to increase at the low values of $\alpha<5°$ along all δ except in the region $75°<\delta<105°$, confirming that the first-layer interatomic spacings are shortest in the region near $\delta=90°$ and very long elsewhere. This flat, featureless structure of the low-α contour results from the insensitivity of α_c to changes in large (> 10 Å) interatomic spacings. (iii) I(BS) is lowest near the $\delta=\pm 35.3°$ and 90° directions and highest near the $\delta=0°$, 65°, and 115° directions. The low intensity near ±35.3° and 90° is due to the alignment of all lattice atoms in the plane of the beam, resulting in relatively more shadowing and blocking of trajectories and limitation to primarily two-dimensional focusing. The higher intensities near 0°, 65°, and 115° result from the fact that atoms in different atomic layers are not aligned in the plane of the beam, thus reducing the amount of shadowing and blocking and enhancing three-dimensional focusing.

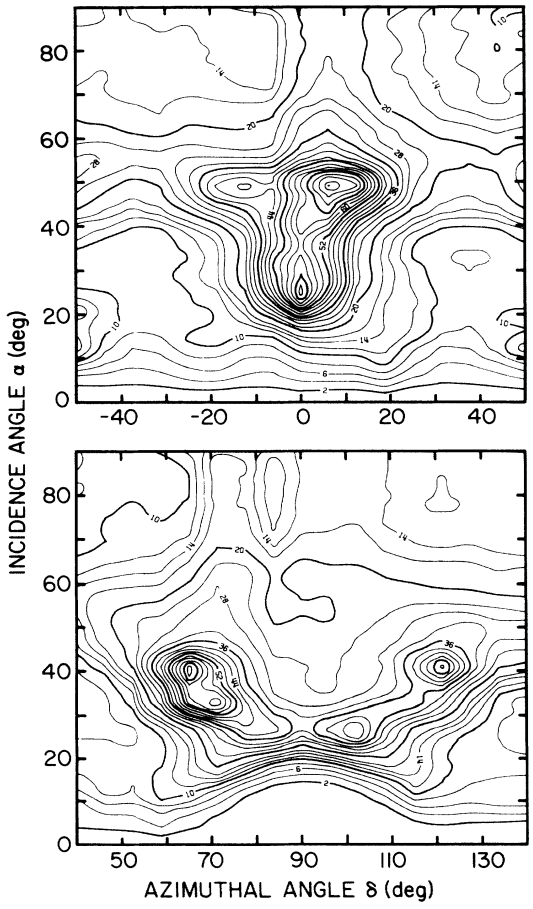

FIG. 5. Scattering structural contour maps (SSCM) of I(BS)x sinα vs δ centered about the [001] ($\delta=0°$) and [1$\bar{1}$0] ($\delta=90°$) azimuths using 4-keV Ar^+ and $\theta=163°$.

E. Forward-scattering intensity I(FS) versus incident angle α scans

When the scattering angle θ is decreased to a forward angle, i.e., <90°, blocking effects contribute significantly to the I(FS) versus α pattern in addition to shadowing effects. In such a case the exit angle $\beta=\theta-\alpha$ is relatively small at high α values, resulting in blocking of some of the scattered trajectories. In this combination *shadowing and blocking mode,* structural features are determined by both the ability of incoming atoms to intersect target atoms and the ability of scattered particles to exit unblocked. The ability to intersect a target atom is determined by α, as described in III C. The ability to escape unblocked is determined by three factors: (i) The maximum available exit angle, β_a. (ii) The distance from the scattering atom to a neighboring blocking atom. (iii) The inclination angle, α_i, i.e., the angle between the surface plane and the line joining the specific scattering and blocking atoms.

I(FS) versus α scans were made for several values of θ between 55° and 85° along the [1$\bar{1}$2] azimuth; three of these are shown in Fig. 6. This azimuth was chosen because all atoms lie in the plane of the beam and a wide trough is formed by the first- and fourth-layer atoms. For $\theta=55°$, only a single intense peak is observed at low α due to focusing of trajectories by first-layer atoms onto first-layer atoms across the trough; the low α_c in the range of 3°–5° is consistent with the large interatomic spacing, i.e., $d>11$ Å, of a faceted (1×3) structure. The shoulder on the low-α side on this peak can be attributed to contributions due to MS, which cannot be resolved from SS at these low θ values, and to surface imperfections.

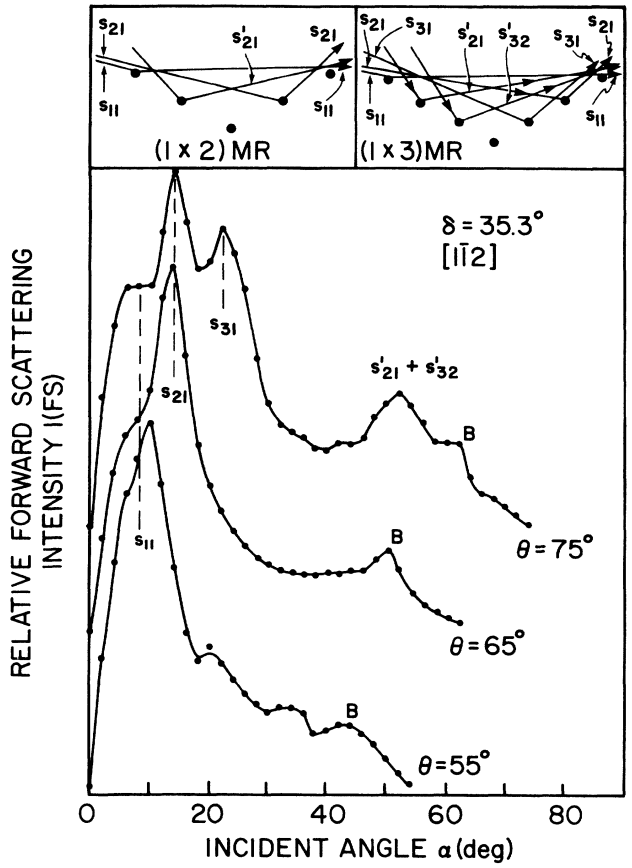

FIG. 6. I(FS) vs incident angle α scans for Ir(110) along the [1$\bar{1}$2] direction for three different θ values. The inset shows the possible quasi-single-scattering trajectories in the FS direction, considering (1×2) (one missing row) and (1×3) (two missing first-layer rows and one missing second-layer row) models. The peaks labeled B are due to focusing by first-layer atoms at the edge of the first-layer blocking cones across the trough along the outgoing trajectories.

Despite the fact that the incoming trajectories at $\theta=55°$ are able to intersect the second (S_{21}) and third (S_{31}) layer atoms at higher α, no such structural features are observed. The reason for this is that the maximum available exit angle β_a is less than the critical exit angle β_c. For example, for $\theta=55°$ the $\alpha_c=12°$, therefore $\beta_a=\theta-\alpha_c=43°$. The $\beta_c=48°$, as will be shown in Sec. III F; it includes the inclination angle, α_i, of the facet to the surface plane and the blocking angle, β_B, of neighboring atoms. Since $\beta_a<\beta_c$, no S_{21} peak is observed. For S_{31}, $\alpha_c=18°$ therefore $\beta_a=37°$. Since $\beta_c=48°$, no S_{31} peak is observed. Table II summarizes this data for several angles θ. The α_c's are smaller than those of Sec. III C due to the significant impact parameter for $\theta<90°$.

As θ increases to 60°, scattered trajectories can escape from both first- and second-layer (S_{11} and S_{21}) scattering and two peaks are observed. Three peaks are observed for $\theta>75°$, where the trajectories can escape from scattering off the first through third layers. The peak centered at $\alpha=52°$ for $\theta=75°$ is due to scattering from second and third layers on the near side of the trough and focusing along the edges of the blocking cones along the outgoing trajectories (S'_{21} and S'_{32}); these trajectories are not possible for $\theta<70°$. The peak labeled B is the highest α structure observed; it is centered at $\approx 13°$ below θ. At this α, scattered trajectories from first-layer atoms on the near side of the trough are focused by blocking cones of first-layer atoms across the trough.

F. Forward-scattering intensity I(FS) versus scattering angle θ scans

Varying θ at constant α provides a scan of the exit angle β. Figure 7 shows such I(FS) versus β scans, where $\beta=\theta-\alpha$, along selected azimuths δ. In this *blocking mode* for FS at low β, the structural features are determined by focusing of scattered trajectories at the edges of the blocking cones of atoms obstructing their escape along that azimuth.

1. First-layer scattering

A low value of $\alpha=8°$ was used so that essentially first-layer scattering is obtained along all azimuths. Thus, the structures are determined by first-layer atoms blocking their first-layer neighbors. The curves of Fig. 7 are normalized to the low-β peak intensity. Data is not shown for $\delta=0°$ and 90° because, along these azimuths, surface semichanneling[26] effects dominate and the intensity of the low-β peak overwhelms that of the high-β peak. This semichanneling is notably lacking at $\delta=46.7°$ because this azimuth is not aligned with the atomic rows, resulting in an abnormally high relative intensity for the high-β peak.

TABLE II. Data from I(FS) versus α scans illustrating the θ values where the S_{21} and S_{31} interactions of Fig. 6 are observed (obs). Note that S_{21} and S_{31} are observed only when $\beta_a \gtrsim \beta_c=48°$.

	Second-layer scattering			Third-layer scattering		
Scattering angle θ	Critical incident angle	Available exit angle β_a	S_{21} obs	Critical incident angle	Available exit angle β_a	S_{31} obs
55°	12.4°	42.6°	No	21.7°	33.3°	No
60°	12.5°	47.5°	Yes	21.9°	38.1°	No
65°	12.6°	52.4°	Yes	22.0°	43.0°	No
70°	12.8°	57.3°	Yes	22.1°	47.9°	Yes
75°	12.9°	62.1°	Yes	22.3°	52.7°	Yes
85°	13.0°	72.0°	Yes	22.5°	62.5	Yes

The two peaks observed in Fig. 7 indicate that there are two different interatomic spacings in the first atomic layer. The peak centered at $\beta=3.5°$ results from a large (> 11 Å) first-layer spacing; its position is relatively constant for different δ because of the low sensitivity to changes in such large interatomic spacings. The peak at higher β results from a small ($\approx$3–9 Å) first-layer interatomic spacing; its position increases with decreasing δ, indicating that this short spacing becomes shorter as δ decreases. This data shows that there are both long and short interatomic spacings in the first atomic layer along [1$\bar{1}$2].

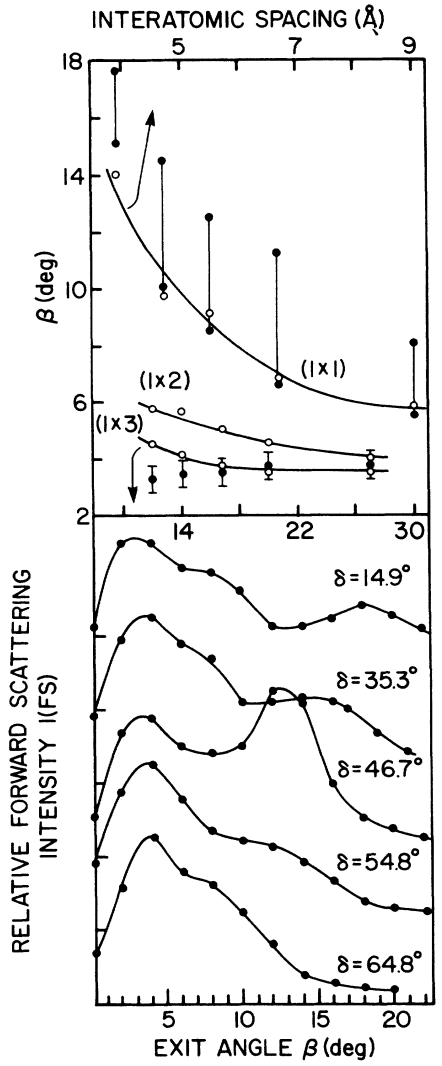

FIG. 7. Lower diagram: I(FS) vs exit angle β scans along five different δ directions with $\alpha=8°$. Upper diagram: Plot of experimental and calculated β vs interatomic spacing d for (1×1), (1×2), and (1×3) structures. The experimental points (solid circles) for the low-α peak are taken as the peak maximum (along with error bars), while those for the high-α peak are drawn as a line from the peak maximum to the half-height position (due to the breadth of the peaks observed). The calculated points (open circles) were obtained from trajectory simulations of the blocking, assuming (1×3), (1×2), and (1×1) structures. The d values for the (1×2) structure are two times those of the (1×1 structure).

The positions expected for these peaks along the different azimuths were estimated from classical simulations of blocking along the outgoing trajectory,[22] assuming (1×1), (1×2), and (1×3) structural models for the first-layer spacings. The results are summarized in the upper part of Fig. 7 as plots of calculated β versus d (i.e., β versus δ) along with the experimental data. The experimental points for the low-β peaks are taken at the peak maximum and error bars are shown. The points for the high-β peaks are shown as lines extending from the peak maximum (maximum β value) to the half-maximum position (minimum β value). The latter positions were determined by curves resolving the two components of the scans. The numbers on the abscissa correspond to first-layer interatomic distances along the azimuths, assuming that there are adjacent (1×1) first-layer rows (upper abscissa) and two missing (1×3) adjacent first-layer rows (lower abscissa). Calculated points assuming zero, one, and two missing rows are indicated. The calculated positions for the (1×3) structure are insensitive to d (or azimuthal direction) and correspond to the position of the low-β peak of Fig. 7. The calculated positions for the (1×1) structure are sensitive to d and correspond to the position of the high-β peak of Fig. 7. The experimental and calculated points are in good agreement for $d>14$ Å and >4 Å for the first and second peaks of Fig. 7, respectively. The poorer agreement at smaller d is a result of deficiencies in the simulations; the calculation considers only pairs of atoms in a plane, which is a poor approximation as δ approaches 90° (smaller d) due to surface semichanneling effects[26] and to the close proximity of off-planar atoms. The calculated positions for a single missing row (1×2) do not agree with either of the observed structures of Fig. 7.

2. *Second-layer scattering*

An I(FS) versus θ scan along the [1$\bar{1}$2] direction with $\alpha=16°$ is shown in Fig. 8. At this high-α value, the incoming trajectories sample both first- and second-layer atoms. The two broad peaks observed at $\beta=6°$ and 16° are due to first-layer atoms blocking their first-layer neighbors in (1×3) and (1×1) structures as in Fig. 7. A low-intensity peak is observed at 48° which corresponds

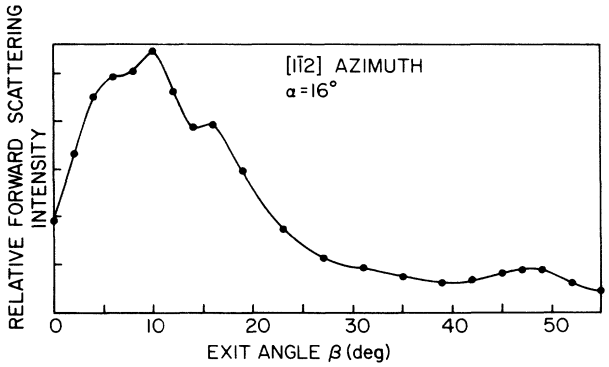

FIG. 8. I(FS) vs β scan along the [1$\bar{1}$2] direction with $\alpha=16°$.

to trajectories scattered from second-layer atoms and focused by blocking cones of their first-layer neighbors across the trough. This defines the critical exit angle $\beta_c = \alpha_i + \beta_B$, i.e., the sum of the inclination angle of the facet and the blocking angle of the neighboring atom, that was used in Sec. III E.

IV. RECONSTRUCTION MODELS

Depictions of different reconstruction models are shown in Fig. 9 as side views along the $[1\bar{1}2]$ azimuth. An unreconstructed (1×1) model is inconsistent with essentially all of the TOF-SARS and LEED results. The only model that is consistent with all of the TOF-SARS and LEED data is one [Fig. 9(a)] that consists of (1×3) faceted structures (two missing first-layer rows and one missing second-layer row) coexisting with minor (1×1) domains (adjacent first-layer rows). Four other models were considered, none of which satisfied all of the experimental data. These will be summarized below.

(1×2) structure. We have recently shown[21] that the reconstructed Ir(110) surface is not a single-missing-row (1×2) structure [Fig. 9(b)] by comparison of the TOF-SARS data to that of Pt(110), which is a documented[1,8,13] (1×2) reconstructed surface. In order to summarize: (i) The LEED pattern is not that of a (1×2) surface; (ii) the I(BS) versus α scans exhibit α_c values characteristic of interatomic spacings with two missing rows and deep layer structures [which are absent in Pt(110)-(1×2)] along [001] and $[1\bar{1}2]$; (iii) along $[1\bar{1}6]$ there is no peak at $\approx 27°$ in the I(BS) versus α scan. This peak, due to the alignment of first-layer atoms with second-layer atoms separated by two atomic rows in a (1×2) structure, is dominant in Pt(110); (iv) the presence of three peaks in the I(FS) versus α scans is consistent with a (1×3) but not a (1×2) structure; (v) the two peaked structure at low α in the I(FS) versus θ scans is inconsistent with a (1×2) structure and consistent with a mixed (1×3) and (1×1) structure.

Two first-layer rows missing. A (1×3) structure which retains the second-layer atom inside the trough [Fig. 9(c)] is inconsistent with the I(BS) versus α scan along $[1\bar{1}6]$; this atom would produce an intense peak at $\alpha \approx 27°$. The I(FS) versus α scans are also inconsistent with this model.

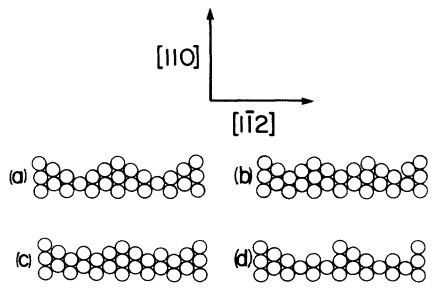

FIG. 9. Reconstruction models considered for Ir(110) shown as side views along the $[1\bar{1}2]$ azimuth. (a) Faceted (1×3) structure with two missing first-layer rows and one missing second-layer row. (b) Single missing row (1×2) structure. (c) (1×3) structure with only two missing first-layer rows. (d) Two first- and second-layer missing-row structures (saw-tooth model).

Consider the β_c and β_a values for a second-layer atom in the center of such a trough. $\alpha_i \approx 10°$ and the interatomic distance between this atom and a first-layer atom is ≈ 7.2 Å, yielding $\beta_B < 15°$, thus $\beta_c < \alpha_i + \beta_B \approx 25°$; $\alpha_c \approx 23°$ for this atom (considering the impact parameter) when $\theta = 55°$, therefore $\beta_a \approx \theta - a_c = 32°$. Since $\beta_a > \beta_c$, an intense peak near $\alpha \approx 23°$ is expected even at low scattering angles ($\theta = 55°$ and 65°) for such a structure; no such peak is observed in Fig. 6.

Two first- and second-layer rows missing (saw tooth). The absence of second-layer atoms on a facet on one side of the trough facilitates BS along $[1\bar{1}2]$ from the fourth-layer atoms that are now exposed. From the trajectory calculations, $\alpha_c \approx 75°$ for such BS. The absence of such a peak in Fig. 4(c) is inconsistent with this structure.

(1×4) structure. A structure with three missing first-layer rows is inconsistent with several aspects of the scans. Most notably, there is no peak at $\sim 27°$ along $[1\bar{1}6]$ (Fig. 4); this peak, due to alignment of first-layer atoms with second-layer atoms separated by two atomic rows, must be present in such a structure. A (1×4) structure with missing second- and third-layer atoms is inconsistent with the FS exit angle scans; the exit angles for such structures would be smaller than those observed.

V. ESTIMATION OF INTERATOMIC SPACINGS

Scattering peaks from the (1×3) domains can be separated from those of the (1×1) domains at low θ. Details of the estimation of the first- to second-layer registry and the first- through fourth-interlayer spacings are presented in this section for the (1×3) domains. Analysis of the (1×1) domains was not attempted because it is a minority structure and its scattering peaks cannot be separated from those of the (1×3) domains. Estimates of the spacings are made from a combination of the experimental measurements and shadow cone calculations.

A. Calibration of interatomic potential

The scaling factor C of the screening function of the Biersack-Ziegler (BZ) potential[28] was adjusted to give the best fit between the computed shadow cone radii R and the experimentally measured radii at a distance L behind the shadowing atom as follows. Trajectory calculations[22] for 4-keV Ar^+ scattering from an Ir atom were carried out for a range of impact parameters p and the cone radii were determined from the envelope of scattered trajectories. Experimental points on the cone radii were determined from α_c's measured from I(BS) versus α scans along $[1\bar{1}0]$ at $\theta = 115°$, 130°, and 163°. α_c was measured at 50% of the peak maximum after background subtraction. Since the interatomic spacing d along the $[1\bar{1}0]$ azimuth is not changed by the reconstruction, it can be used for calibration of the potential. The experimental R, L values were calculated as

$$R = d \sin\alpha_c + p \quad \text{and} \quad L = d \cos\alpha_c \ , \tag{1}$$

where $d = 2.72$ Å is the first-layer interatomic distance along $[1\bar{1}0]$ and p is calculated for the different scattering angles θ as summarized in Table III. The optimum fit of

TABLE III. Summary of the data for calibration of the screening constant of the Biersack-Ziegler potential.

θ	p (Å)	α_c	R (Å)	σ (Å)
115°	0.14	20.3°	1.09	
130°	0.11	20.6°	1.07	0.012
163°	0.03	22.7°	1.09	

the calculated radii to the experimental (R,L) points was obtained for $C=0.81$ with a standard deviation of $\sigma=0.012$ Å in R.

Due to reconstruction, d along other azimuths (providing different L values) cannot be used for calibration. Nevertheless, we expect the C value determined above to be accurate for the following reasons. First, the three experimental points at one L value (same azimuth) corresponding to three different θ (or p) are within 0.02 Å of each other, showing that the experimental measurements are reproducible. Second, the systematic error caused by the lack of points at different L is expected to be small. For 4-keV Ar^+ scattering from W, $C=0.85$ as calibrated from seven experimental points.[22] Since the energies and masses involved in the present case are similar, the C values are expected to be very close. The difference in $C=0.81$ and 0.85 gives an uncertainty of <0.03 Å in the measurement of interatomic spacings.

B. Lateral shifts—first- to second-layer registry

The possibility of a shift in the first- to second-layer registry was investigated by monitoring α_c for second-layer scattering, i.e., the (001)-($\frac{1}{2}\frac{1}{2}2$) interaction, from $I(S)$ versus α scans along azimuths near [1$\bar{1}$2]. If there are no shifts, the maximum α_c should occur at the bulk value of $\delta=35.3°$. Scattering angles of 70° and 115° were used, although possible problems exist for both of them. At $\theta=115°$, the I(BS) versus α scans can contain contributions from third- and fourth-layer scattering which are accessible at similar α values as second-layer scattering. At $\theta=70°$, such deep layer scattering is blocked, however, the large p value associated with FS results in a lower sensitivity to the atomic core and multiple-scattering contributions can be as high as ~30% of I(FS). Figure 10 shows a plot of α_c versus δ near the [1$\bar{1}$2] direction for $\theta=115°$. A maximum is observed at $\delta_{max}=33.0°$, indicating that the second-layer atom is shifted towards the center of the trough along the [001] coordinate. Assuming no shifts along the [1$\bar{1}$0] direction, the [001] coordinate of the second-layer atom is estimated as $1.36/\tan\delta_{max}=2.09$ Å, i.e., a shift of 0.17 Å from the bulk value. Using the 70° data, $\delta_{max}=34.3°$ resulting in an [001] coordinate of 1.99 Å and a shift of 0.07 Å from the bulk value. These measurements are in qualitative agreement that there is a lateral shift in the second layer, the estimated average value being $\sim 0.12\pm0.10$ Å. The ±0.10 Å uncertainty corresponds to a maximum error of $\pm1.5°$ in δ_{max} resulting from uncertainties in determining α_c and calibration of δ.

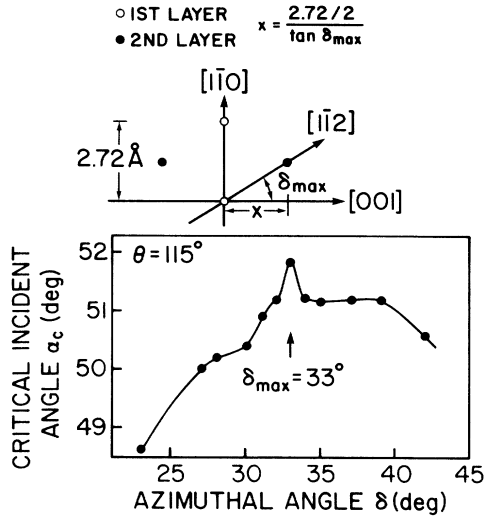

FIG. 10. Plot of α_c [determined from I(BS) vs α plots] vs δ in the region near the [1$\bar{1}$2] azimuth where first- to second-layer atom alignment is expected. The inset illustrates the estimation of the [001] coordinate of the second-layer atom.

C. Vertical shifts

1. First- to second-layer spacing

The I(FS) versus α scan along [1$\bar{1}$2] using $\theta=70°$ was used for an estimation of the first- to second-layer spacing z_{12}. Since the [001] coordinate of the second-layer atom was determined in Sec. V B and the shadow cone radius $R(L)$ was calibrated in Sec. V A, z_{12} can be estimated as shown in Fig. 11 from

$$R'(L)=A\sin(\alpha_c-\alpha_i)+p \text{ and } L=A\cos(\alpha_c-\alpha_i)\,, \quad (2)$$

where α_c is determined from the (001)-($\frac{1}{2}\frac{1}{2}2$) scattering peak, A is the distance between a first- and second-layer atom, and $\alpha_i=\tan^{-1}(z_{12}/d)$. The procedure used is to first assume a z_{12} value, calculate A, and then calculate $R'(L)$ and L from Eq. (2). $R'(L)$ is then compared to $R(L)$ at the appropriate L value and z_{12} is incremented appropriately until $R'(L)=R(L)$. The result is

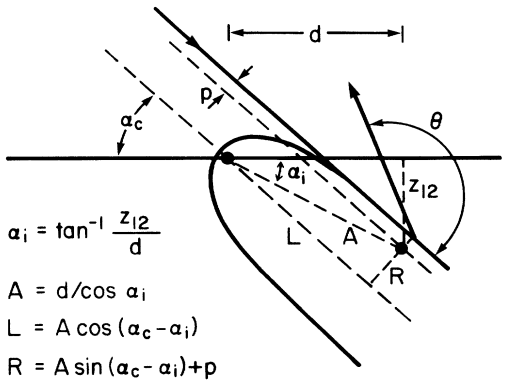

FIG. 11. Schematic drawing showing the use of the calculated shadow cone and experimental α_c value for second-layer scattering in estimating the first- to second-layer vertical spacing z_{12}.

$z_{12} \sim 1.25 \pm 0.10$ Å, i.e., a contraction of 0.11 Å from the bulk value. The parameters used in the calculation are summarized in Table IV. z_{12} was also estimated from the (001)-($\frac{1}{2}\frac{1}{2}2$) peak using $\theta = 115°$ and from the (001)-($\frac{5}{2}\frac{5}{2}2$) peak using $\theta = 65°$ and 80°. Although these measurements are not considered to be as accurate as the one described above (because of deep layer contributions in the former case and the large distance between the shadowing and scattering atom in the latter case), there is qualitative agreement between them as shown in Table IV.

2. *First- to third-layer spacing*

The first- to third-layer spacing z_{13} was estimated from the α_c of the (001)-(203) peak at $\alpha = 29°$ in the I(BS) versus α scans along [001] using $\theta = 115°$ and 130°. The $\theta = 163°$ scan was not used because of contributions from deeper layers and at the $\alpha = 29°$ position. Also, the separation of this peak from the $\alpha \approx 20°$ peak is improved at smaller θ due to the lower background from the reduced deep layer scattering. The results, listed in Table IV, provide an estimate of z_{13} as $\sim 2.61 \pm 0.10$ Å, which is smaller than the bulk value by 0.11 Å. Considering that z_{12} is contracted by ~ 0.11 Å, the second to third-layer spacing is $z_{23} = z_{13} - z_{12} \sim 1.36$ Å, i.e., equivalent to the bulk spacing. The (001)-(103) peak was not used in this determination because of overlap with the ($\frac{1}{2}\frac{1}{2}2$)-($\frac{3}{2}\frac{1}{2}4$) peak.

3. *First- to fourth-layer spacing*

The first- to fourth-layer spacing z_{14} was estimated from the α_c of the (001)-($\frac{3}{2}\frac{1}{2}4$) peak at $\alpha \sim 45°$ in the I(BS) versus α scans along [1$\bar{1}$6] using $\theta = 163°$ and 130°. The results, listed in Table IV, provide an estimate for Z_{14} as $\sim 3.96 \pm 0.10$ Å, which is smaller than the bulk value by 0.12 Å. Hence, the third- to fourth-layer spacing is $z_{34} = z_{14} - z_{12} - z_{23} \sim 1.35$ Å, i.e., equivalent to the bulk spacing.

VI. DISCUSSION

The TOF-SARS data are only consistent with one of the reconstruction models that we have considered. This model consists of primary faceted (1×3) domains and coexisting secondary (1×1) domains. TOF-SARS is not capable of determining how many adjacent [1$\bar{1}$0] rows exist together in the (1×1) domains; it only shows that there are some first-layer spacings that correspond to the 3.84-Å lattice constant along the [001] direction, while others correspond to three times that number. This shows that, under this annealing condition, the Ir(110) reconstruction is not complete, i.e., not all of the unreconstructed (1×1) surface is converted into (1×3) domains. Thus, there is considerable disorder along the [001] direction due to the different atomic row spacings. This disorder is consistent with the streaked LEED patterns.

Analysis of the (1×3) domains shows that (i) the second-layer atoms in the facet shift laterally towards the center of the trough, the estimated shift being $\sim 0.12 \pm 0.10$ Å, (ii) the first- to second-layer spacing is contracted from the bulk value, the estimated contraction being $\sim 8\%$, and (iii) the second- to third- and third- to fourth-layer spacings are similar to the bulk values. This analysis is complicated by the open structure of the Ir(110) reconstructed surface. The accuracy of the interatomic spacings is affected by the following factors. (i) Only the limited α_c's along the [1$\bar{1}$0] azimuth are useful for calibration, (ii) due to the exposed first- through fourth-layer atoms, there are many peaks in the I(BS) versus α scans and some of these overlap, (iii) deep layer scattering (from below the fourth-layer) can produce peaks that interfere with the outer-layer α_c's, (iv) focus-

TABLE IV. Summary of the data used for the determination of the first- through fourth-layer spacings, z_{ij}.

	Shadowing-scattering atoms			
θ (deg)	(001)-($\frac{1}{2}\frac{1}{2}2$)	(001)-($\frac{5}{2}\frac{5}{2}2$)	z_{12} (Å)	$\bar{z}_{12}$ (Å)
	α_c	α_c		
70°	46.2°		1.25	
65°		11.4°	1.22[a]	1.25±0.10
80°		11.9°	1.22[a]	
115°	51.5°		1.32[a]	
	(001)-(203)		z_{13} (Å)	$\bar{z}_{13}$ (Å)
	α_c			
115°	27.5°		2.61	2.62±0.10
130°	28.0°		2.64	
	(001)-($\frac{3}{2}\frac{1}{2}4$)		z_{14} (Å)	$\bar{z}_{14}$ (Å)
	α_c			
130°	44.3°		4.01	3.96±0.10
163°	44.2°		3.92	

[a]These values are not used due to the uncertainties discussed in the text.

ing effects attenuate as the distance between the shadowing and scattering atoms increases, producing broader I(BS) versus α structures, and (v) the coexistence of (1×3) and (1×1) structures adds complexity.

The TOF-SARS and LEED data complement each other. LEED is sensitive to long-range order, i.e., minimum domain size of 100–200 Å, and provides a direct measurement of surface symmetry in reciprocal space. TOF-SARS is sensitive to short-range order, i.e., individual interatomic spacings along azimuths, and provides a direct measurement of interatomic distances in the first and subsurface layers in real space. The complementary nature of these techniques is exemplified in this Ir(110) work. The LEED data suggest a disordered $(1\times n)$ structure, whereas the TOF-SARS data confirm the coexistence of (1×1) and (1×3) structures.

VII. SUMMARY

The TOF-SARS and LEED data agree that after annealing the Ir(110) surface to 1400 °C and cooling to room temperature, the surface is reconstructed into major (1×3) domains and minor (1×1) domains. The data are consistent with a model in which the major faceted (1×3) structures have two missing first-layer rows and one missing second-layer row in the center of the trough and the minor (1×1) structures have two or more adjacent first-layer rows. Analysis of the (1×3) structure indicates a lateral shift of the second-layer atoms, estimated to be $\sim0.12\pm0.10$ Å (6% of the bulk value), towards the center of the trough and a contraction of the first- to second-layer vertical spacing, estimated to be $\sim0.11\pm0.10$ Å (8% of the bulk value). The second- through fourth-layer spacings appear to be unchanged from the bulk values within the accuracy of the measurement, i.e., ±0.10 Å.

ACKNOWLEDGMENTS

This material is based on work supported by the National Science Foundation under Grant No. CHE-88-14337. The authors are grateful to R. R. Rye (Sandia National Laboratories) for stimulating our interest in this surface, for providing the Ir crystal, and for helpful discussions.

[1]T. Gustafsson, M. Copel, and P. Fenter, in *The Structure of Surfaces II,* edited by J. F. van der Veen and M. A. Van Hove (Springer, Berlin, 1988), p. 110.

[2]P. Häberle, P. Fenter, and T. Gustafsson, Phys. Rev. B **39**, 5810 (1989).

[3]J. W. M. Frenken, R. L. Krans, J. F. van der Veen, E. Houlb-Krappe, and K. Horn, Phys. Rev. Lett. **59**, 2307 (1987).

[4]K.-M. Ho and K. P. Bohnen, Phys. Rev. Lett. **59**, 1833 (1987).

[5]K. W. Jacobsen and J. K. Nørskov, in *The Structure of Surfaces II,* edited by J. F. van der Veen and M. A. Van Hove (Springer-Verlag, Berlin, 1987), p. 118.

[6]M. S. Daw, Surf. Sci. **166**, L161 (1986).

[7]V. Heine and L. D. Marks, Surf. Sci. **165**, 65 (1986).

[8]E. C. Sowa, M. A. Van Hove, and D. L. Adams, Surf. Sci. **199**, 174 (1988); P. Fery, W. Moritz, and D. Wolf, Phys. Rev. B **38**, 7275 (1988); D. L. Adams, H. B. Nielsen, M. A. Van Hove, and A. Ignatiev, Surf. Sci. **104**, 47 (1981).

[9]C. M. Chang, M. A. Van Hove, W. H. Weinberg, and E. D. Williams, Surf. Sci. **91**, 440 (1980); M. A. Van Hove, W. H. Weinberg, and C. M. Chang, in *Low Energy Electron Diffraction: Experiment, Theory, and Surface Structure Determination,* Vol. 6 of *Springer Series in Surface Sciences,* edited by M. A. Van Hove (Springer, Berlin, 1986); C.-M. Chang and M. A. Van Hove, Surf. Sci. **171**, 226 (1986).

[10]K. Christmann and G. Ertl, Z. Naturforsch. **28a**, 144 (1973).

[11]Q. J. Gao and T. T. Tsong, J. Vac. Sci. Technol. A **15**, 761 (1987); K. Müller, J. Witt, and O. Schütz, *ibid.* **5**, 757 (1987); G. L. Kellogg, *ibid.* **5**, 747 (1987).

[12]T. E. Jackman, J. A. Davies, D. P. Jackson, P. R. Norton, and W. N. Unertl, J. Phys. C **15**, L99 (1982); Surf. Sci. **120**, 389 (1982).

[13]H. Niehus, Surf. Sci. **145**, 407 (1984).

[14]J. Möller, K. J. Snowdon, W. Heiland, and H. Niehus, Surf. Sci. **176**, 475 (1986).

[15]S. H. Overbury, W. Heiland, D. M. Zehner, S. Datz, and R. S. Thoe, Surf. Sci. **109**, 293 (1981).

[16]P. Häberle, P. Fenter, and T. Gustafsson, Phys. Rev. B **39**, 5810 (1989); M. Copel, P. Fenter, and T. Gustafsson, J. Vac. Sci. Technol. A **5**, 742 (1987).

[17]I. K. Robinson, Phys. Rev. Lett. **50**, 1145 (1983).

[18]L. D. Marks, Phys. Rev. Lett. **51**, 1000 (1981).

[19]G. Binnig, H. Rohrer, Ch. Gerber, and E. Weibel, Surf. Sci. **131**, L379 (1983).

[20]W. Hetterich and W. Heiland, Surf. Sci. **210**, 129 (1989).

[21]H. Bu, M. Shi, F. Masson, and J. W. Rabalais, Surf. Sci. **230**, L140 (1990).

[22]O. Grizzi, M. Shi, H. Bu, J. W. Rabalais, and P. Hochmann, Phys. Rev. B **40**, 10 127 (1989).

[23]H. Bu, O. Grizzi, M. Shi, and J. W. Rabalais, Phys. Rev. B **40**, 10 147 (1989).

[24]M. Shi, O. Grizzi, H. Bu, J. W. Rabalais, R. R. Rye, and P. Nordlander, Phys. Rev. B **40**, 10 163 (1989).

[25]J. W. Rabalais, O. Grizzi, M. Shi, and H. Bu, Phys. Rev. Lett. **63**, 51 (1989); O. Grizzi, M. Shi, H. Bu, J. W. Rabalais, R. R. Rye, and P. Nordlander, *ibid.* **63**, 1408 (1989)

[26]O. Grizzi, M. Shi, H. Bu, and J. W. Rabalais, Rev. Sci. Instrum. **61**, 740 (1990).

[27]J. W. Rabalais, CRC Critical Rev. Solid State Mater. Sci. **14**, 319 (1989).

[28]J. F. Zeigler, J. P. Biersack, and U. Littmark, *The Stopping and Range of Ions in Solids* (Pergamon, New York, 1985).

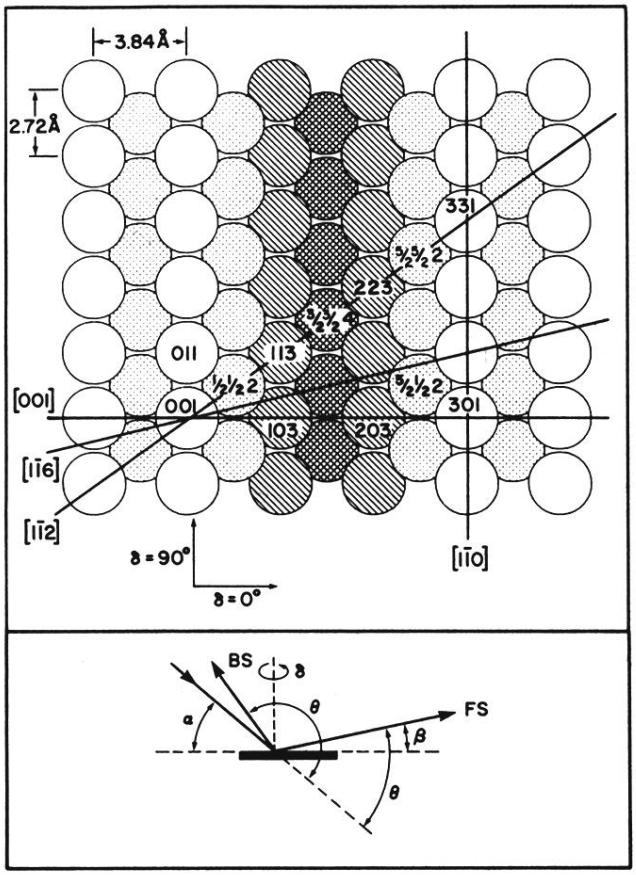

FIG. 1. Reconstructed Ir(110) surface showing coexisting faceted (1×3) and (1×1) structures. Open circles, first layer; dotted circles, second layer; dashed circles, third layer; hatched circles, fourth layer. The nomenclature for the atomic positions is indicated. The angular notation used in TOF-SARS is shown in the lower figure.

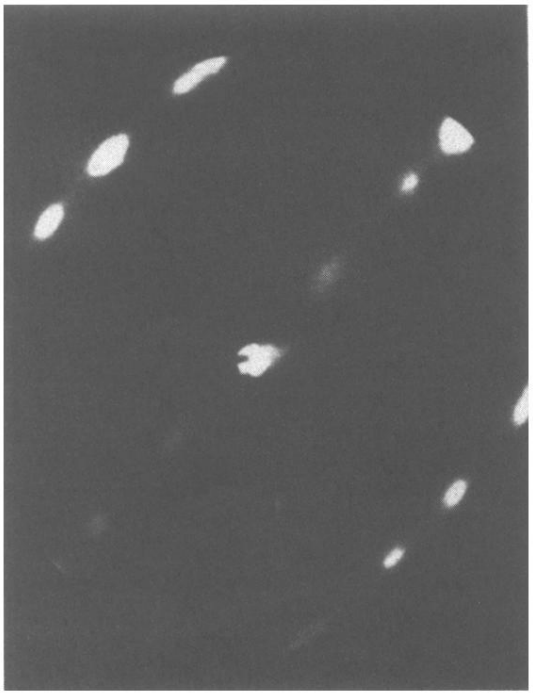

FIG. 2. LEED pattern observed for clean Ir(110) after annealing to 1400 °C.